CRYSTALLINE COLLOIDAL ARRAY FILTER AND RAMAN IMAGING

By

Xing Chao

BS, Nanjing University, 2010

Submitted to the Graduate Faculty of

The Kenneth P. Dietrich School of Arts and Sciences in partial fulfillment

of the requirements for the degree of

Master of Science

University of Pittsburgh

2012

UNIVERSITY OF PITTSBURGH

Kenneth P. DIETRICH SCHOOL OF ARTS AND SCIENCES

This Master degree thesis was presented

by

Xing Chao

It was defended on

November 19, 2012

and proved by

Sanford A. Asher, PhD, Professor

David H. Waldeck, PhD, Professor

Nathaniel L. Rosi, PhD, Associate Professor

Thesis Director: Sanford A. Asher, PhD, Professor

CRYSTALLINE COLLOIDAL ARRAY FILTER AND RAMAN IMAGING

Xing Chao, M. S.

University of Pittsburgh, 2012

The background and diffraction theory of crystalline colloidal arrays (CCAs) are briefly reviewed. Crystalline colloidal arrays were fabricated by using silica particles and polystyrene (PS) particles for deep ultraviolet (UV) and visible regions, respectively. I used a modified Stöber method to synthesize small (<100 nm) silica particles. The silica particles were surface functionalized with a strong acid, non-UV absorbing silane coupling agent. PS particles were also synthesized with emulsion polymerization method. These monodisperse, highly charged particles self-assemble into face-centered cubic CCAs that show Bragg diffraction of UV and visible light. The diffraction wavelength was 248 nm for silica CCA filter at normal incidence. The PS CCAs diffracted 518 nm and 580 nm light at normal incidence.

These CCA filters were tested with UV/vis/NIR spectrophotometer and lasers. UV/vis/NIR extinction showed high rejection efficiency and narrow diffraction bands. 244 nm argon laser light was used to study the transmission, reflection and scattering of the silica CCA filter. Teflon Raman scattering measurement was also performed with 244 nm light and a silica CCA filter used as the Rayleigh rejection filter. The filter rejected 99.91% of the Rayleigh scattering light.

We attempted to develop a Raman imaging spectrometer. Towards this affect, I attempted to do fluorescence imaging by using 514.5 argon laser light with PS visible filters. Spectra of fluorescence bands and fluorescence images were recorded.

Key Words: crystalline colloidal arrays, photonic crystals, silica colloidal, polystyrene colloidal, UV Raman imaging, Raman spectroscopy, Rayleigh rejection filter, wavelength-selecting filter.

TABLE OF CONTENTS

LIST OF FIGURES

LIST OF EQUATIONS

1. Introduction and Background

1.1. Crystalline Colloidal Array (CCA) and Applications

Looking around at the colorful nature surrounding us, there are two ways nature presents color to us. One is through iridescent pigments, which changes the color of reflected or transmitted light. The other is through structural colored materials, which are not colored themselves, but diffract the light of specific wavelengths to give iridescent colors.

Photonic crystals are artificial color structures, which have periodic dielectric structures with refractive index contrast, designed to control photon propagation in the same way that semiconductor crystals control electron propagation. In other words, it appears allowed bands and forbidden gaps for photons (Fig. 1) [1].

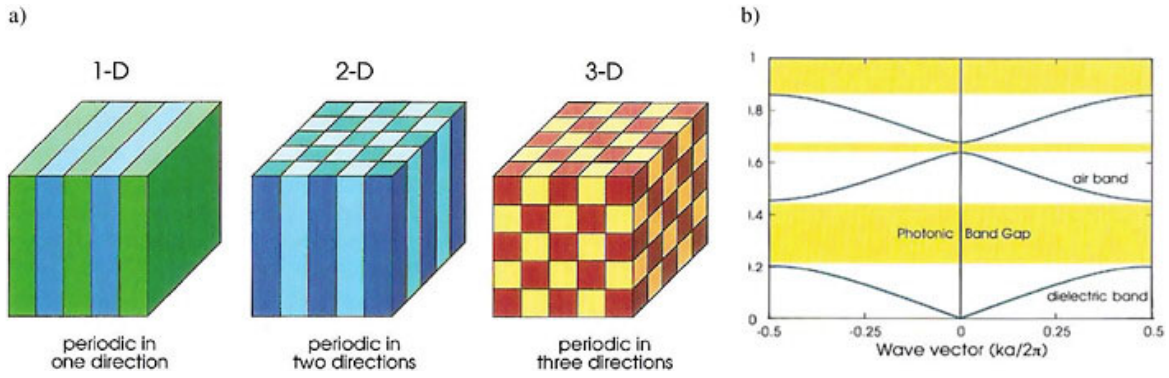

Fig. 1. a) 1-D, 2-D and 3-D periodicity and b) photonic band gap in 1-dimensional. (From Ref. 1)

Although photonic crystals have been studied in one form or another since 1887, the term "photonic crystal" was first used in two milestone papers by Eli Yablonovitch and Sajeev John on photonic crystals in 1987 [2, 3]. After that, the study of photonic crystals is of intense interests, and the number of research papers about photonic crystals started to grow exponentially.

Crystalline colloidal arrays (CCAs) are ordered arrays of colloid particles, that are analogous to atomic and molecular crystals. The arrays can be periodic in one-dimension, two-dimensions and three-dimensions.

Fig. 1 shows a schematic view of the different periodicity. Nature shows a lot of examples of crystalline colloidal arrays, such as the gem opal, in which spheres of silica assume a close-packed periodic structure under moderate compression [4]; the wings of morpho butterflies, which exhibit brilliant blue structural colors even without an angular dependence [5]. In the lab, CCAs are formed by self assembly of colloidal particles into ordered crystalline structures [6].

CCAs have found application in optics such as photonic band gap crystals (PBGCs) [7]. Also, CCAs are used in the field of material science as templates [8]. The optical properties of CCAs depend on many parameters, such as particle size, number concentration and degree of regularity. They diffract light at specific wavelength that meets the Bragg condition, and the specific wavelength diffracted is sensitive to the particle spacing of the CCA, which makes CCA a great sensing motif. As a world leading group in research of CCA, our group developed sensors for many analytes, such as pH [9, 10], metal ions [11], ethanol [10] , glucose [12] and antibodies [13], by embedding the CCA into functional hydrogels. With hydrogel swelling and shrinking, the particle spacing of CCA changes and the diffracted light wavelength shifts to indicate different analyte concentrations.

The diffracted wavelength changes continuously with the incident glancing angle of CCA. Taking advantage of this tunable rejection band, our group has developed CCA rejection filters for different wavelength ranges. In the late 1980's, we developed the first photonic crystal device for Raman spectroscopy [14, 15]. This optical device, which functioned as a Bragg diffraction filter, was fabricated from a CCA of ~100 nm diameter highly charged, monodisperse polystyrene (PS) particles. These highly charged particles self assembled into a face centered cubic (fcc) structure that efficiently Bragg diffracts light in visible range from its (111) planes [14], but freely transmitted light in adjacent spectral regions. This optic functioned as a highly efficient Rayleigh rejection filter for Raman spectral measurements. This photonic crystal device was licensed and commercialized. The recent development of highly efficient holographic filters and multilayer dielectric filters has dramatically advanced near UV, visible and near IR

spectroscopies [16, 17, 18]. Unfortunately, because of the typical materials used to fabricate those devices usually absorb deep UV light, similar devices do not exist in the deep UV range [19, 20].

Recently, we developed an analogous photonic crystal device that functioned as an efficient Bragg diffraction filter in the deep UV [21]. This deep UV CCA filter was fabricated from ~50 nm diameter monodisperse highly charged silica particles. This deep UV CCA filter was demonstrated to be a Rayleigh rejection filter in deep UV Raman measurements.

The work here is to closely study and reveal the properties of CCA filters. I also attempted to build a hyperspectral spectrometer with the CCA filters. Fluorescence imaging was demonstrated here as a showcase of Raman imaging.

1.2 Diffraction from Crystalline Colloidal Array

CCAs are analogous periodic materials with standard atomic and molecular crystal. By understanding the fundamental theories of diffraction from atomic and molecular crystals, we can obtain important knowledge about diffraction from CCAs. The following sections follow and adapt the formalism of Kittle [22], Cowley [23] and Zachariasen [24] to reveal the essential properties of periodic materials.

1.2.1. Reciprocal Lattice and Miller Indices

Materials that have periodic arrays of particles are called crystals. The crystal structure consists of thee periodicity of the lattice and the basis. If we have a function $f(\boldsymbol{r})$ that is periodic on a lattice; that is, suppose $f(\boldsymbol{r}) = f(\boldsymbol{r} + \boldsymbol{R})$ for all vectors $\boldsymbol{R}$ that translate the lattice into itself. The vectors $\boldsymbol{R}$ here are called the lattice vectors. The function $f(\boldsymbol{r})$ can be the electron density function $n(\boldsymbol{r})$ for atomic crystal; in the photonic crystal system it can be the dielectric function $\varepsilon(\boldsymbol{r})$.

Dealing with a periodic function, a natural thing to do is to take the Fourier transform. We can build the periodic function $f(\boldsymbol{r})$ in the form of plane waves with various wave vectors:

$$f(\boldsymbol{r}) = \int d^3\boldsymbol{q} g(\boldsymbol{q}) e^{i\boldsymbol{q}\cdot\boldsymbol{r}} \quad (1)$$

Here $g(\boldsymbol{q})$ is the coefficient of the plane wave with wave vector $\boldsymbol{q}$. Moreover, the function f here requires the periodicity on the lattice, which is $f(\boldsymbol{r}) = f(\boldsymbol{r} + \boldsymbol{R})$. The expansion will end up being:

$$f(\boldsymbol{r} + \boldsymbol{R}) = \int d^3\boldsymbol{q} g(\boldsymbol{q}) e^{i\cdot\boldsymbol{q}\cdot\boldsymbol{r}} e^{i\cdot\boldsymbol{q}\cdot\boldsymbol{R}} = f(\boldsymbol{r}) = \int d^3\boldsymbol{q} g(\boldsymbol{q}) e^{i\boldsymbol{q}\cdot\boldsymbol{r}} \quad (2)$$

The periodic nature of f convince its Fourier transform $g(\boldsymbol{q})$ to have the special property $g(\boldsymbol{q}) = g(\boldsymbol{q})\exp(i\boldsymbol{q}\cdot\boldsymbol{R})$. However, this property requires $g(\boldsymbol{q}) = 0$ or $\exp(i\boldsymbol{q}\cdot\boldsymbol{R}) = 1$, in other words, the transform $g(\boldsymbol{q})$ is zero everywhere, except for spikes at the values of $\boldsymbol{q}$ such that $\exp(i\boldsymbol{q}\cdot\boldsymbol{R}) = 1$ for all $\boldsymbol{R}$.

Those vectors $\boldsymbol{q}$ such that $\exp(i\boldsymbol{q}\cdot\boldsymbol{R}) = 1$, which are equivalent with $\boldsymbol{q}\cdot\boldsymbol{R} = 2\pi N$ (N is an integer), are called reciprocal lattice vectors and are usually designated as $\boldsymbol{G}$. The reciprocal lattice vectors form a lattice of in reciprocal space, which is also called momentum space or k-space, in responding to the lattice vectors $\boldsymbol{R}$. So it is possible to build the periodic function $f(\boldsymbol{r})$ with an appropriate weighted sum over all of the reciprocal lattice vectors, as follows:

$$f(\boldsymbol{r}) = \sum_{\boldsymbol{G}} f_{\boldsymbol{G}} e^{i\boldsymbol{G}\cdot\boldsymbol{r}}. \quad (3)$$

where f_{G} is the Fourier coefficient.

Every lattice vector $\boldsymbol{R}$ can be written in terms of the primitive lattice vectors, which are the smallest vectors pointing from one lattice point to another. For example, in a simple cubic lattice with lattice constant a, the vector $\boldsymbol{R}$ will all be of the form $\boldsymbol{R} = h'a\hat{\boldsymbol{x}}+k'a\hat{\boldsymbol{y}}+l'a\hat{\boldsymbol{z}}$, where ($h'$, k', l') are integers. In general, we call the primitive lattice vectors $\boldsymbol{a}_1$, $\boldsymbol{a}_2$ and $\boldsymbol{a}_3$, which need not be of unit length.

Given a lattice with a set of lattice vectors $\boldsymbol{R}$, we need to find all the reciprocal lattice vectors $\boldsymbol{G}$ such that $\boldsymbol{G}\cdot\boldsymbol{R}$ is some integer multiple of 2π for every $\boldsymbol{R}$. The reciprocal lattice has a set of primitive vectors $\boldsymbol{b}_j$ as well, so that every reciprocal lattice vector $\boldsymbol{G}$ can be written as $\boldsymbol{G} = h\boldsymbol{b}_1+k\boldsymbol{b}_2+l\boldsymbol{b}_3$, where ($h$, k, l) are integers. With the requirement that $\boldsymbol{G}\cdot\boldsymbol{R} = 2\pi N$ (N is integer), we have:

$$\boldsymbol{G}\cdot\boldsymbol{R}=(h'\boldsymbol{a}_1+k'\boldsymbol{a}_2+l'\boldsymbol{a}_3)\cdot(h\boldsymbol{b}_1+k\boldsymbol{b}_2+l\boldsymbol{b}_3)=2\pi N \quad (4)$$

In order to satisfy the above equation, $\boldsymbol{b}_j$ is constructed in the way that $\boldsymbol{a}_i\cdot\boldsymbol{b}_j=2\pi$ if $i=j$, and 0 if $i \neq j$. In a more compact format, it can be written as $\boldsymbol{a}_i\cdot\boldsymbol{b}_j = 2\pi\delta_{ij}$. Thus, the primitive reciprocal lattice vectors can be constructed as below:

$$\boldsymbol{b}_1=\frac{2\pi\boldsymbol{a}_2\times\boldsymbol{a}_3}{\boldsymbol{a}_1\cdot(\boldsymbol{a}_2\times\boldsymbol{a}_3)},\quad \boldsymbol{b}_2=\frac{2\pi\boldsymbol{a}_3\times\boldsymbol{a}_1}{\boldsymbol{a}_1\cdot(\boldsymbol{a}_2\times\boldsymbol{a}_3)},\quad \boldsymbol{b}_3=\frac{2\pi\boldsymbol{a}_1\times\boldsymbol{a}_2}{\boldsymbol{a}_1\cdot(\boldsymbol{a}_2\times\boldsymbol{a}_3)}. \quad (5)$$

The primitive reciprocal lattice vectors define the reciprocal lattice. The reciprocal lattice plays a fundamental role in most studies of periodic structure, particularly in the theory of diffraction. The diffraction pattern of a crystal can be used to determine the reciprocal lattice vectors, and then reveal the atomic arrangement of a crystal, which is also true for photonic crystals.

A set of lattice planes is determined by the three integers (*h*,*k*,*l*), which are known as the Miller indices. Each index denotes a plane orthogonal to a direction (*h*,*k*,*l*) in the basis of the reciprocal lattice vectors. Miller indices form a notation system in crystallography for planes and directions in crystal lattices.

There are two equivalent ways to determine the Miller indices for crystal planes: via a point in the reciprocal lattice, or as inverse intercepts along the lattice vectors.

With the primitive reciprocal lattice vectors determined above, it is easy to write the reciprocal lattice vector as: $\boldsymbol{G}_{hkl}=h\boldsymbol{b}_1+k\boldsymbol{b}_2+l\boldsymbol{b}_3$, the three indices *h*, *k*, *l* are the Miller indices, (*hkl*) denotes planes orthogonal to the reciprocal lattice vector. And (*hkl*) indicates a normal to the planes in the basis of the primitive reciprocal lattice vectors.

Equivalently, (*hkl*) denotes a plane that intercepts the three points $\boldsymbol{a}_1/h$, $\boldsymbol{a}_2/k$, $\boldsymbol{a}_3/l$, or some multiple thereof. That indicates the Miller indices are proportional to the inverse of the intercepts of the plane, in the basis of the lattice vectors. If one of the indices is zero, it means that the planes do not intersect that axis. Fig.2 gives a clear view of planes with different Miller indices. [25]

The Miller indices are very important and convenient in crystallography. It provides an easy way to find the specific planes and planes spacing in the crystal. Considering only (*hkl*) planes intersecting one or more lattice points, the perpendicular distance *d* between adjacent lattice planes is related to the reciprocal lattice vector orthogonal to the planes by: $d = 2\pi/|\boldsymbol{G}_{hkl}|$. For cubic crystal with lattice constant *a*, the spacing *d* between adjacent (*hkl*) lattice planes is $d_{hkl} = \frac{a}{\sqrt{h^2+k^2+l^2}}$.

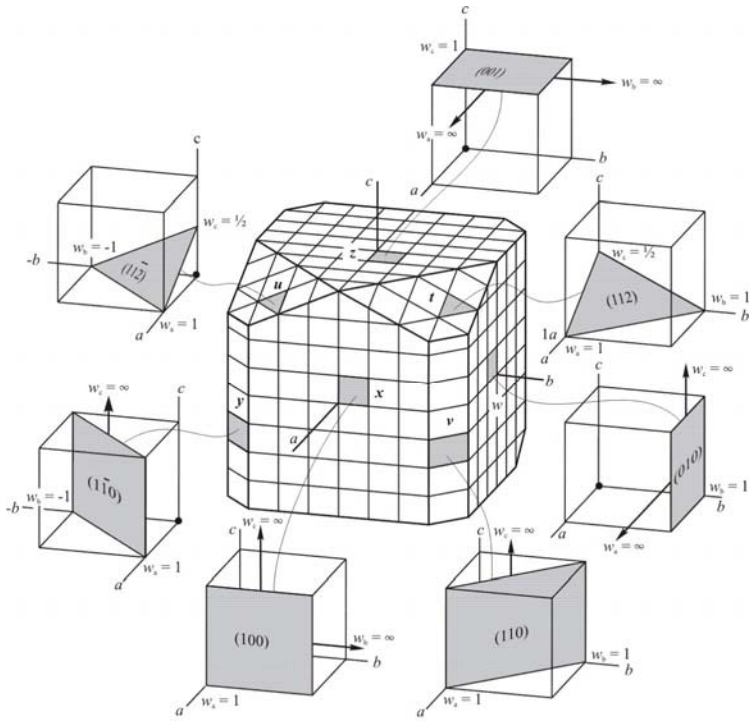

Fig. 2. Examples of different lattice planes and their Miller indices. From Ref. 25.

1.2.2. Kinematical Diffraction Theory

If the amplitude of a wave scattered by lattice points is much less than the incident wave amplitude, we can assume as a first approximation that the amplitude of wave function $\psi(\boldsymbol{r})$, which is the wave function in scattering filed, may be replaced by $\psi^{(0)}(\boldsymbol{r})$, which is the incident wave amplitude. This is the "First Born Approximation". For higher order Born approximations, $\psi(\boldsymbol{r}) = \psi^{(0)}(\boldsymbol{r}) + \psi^{(1)}(\boldsymbol{r}) + \psi^{(2)}(\boldsymbol{r}) + \cdots$.

The first Born approximation for scattering from a three-dimensional distribution, known as the "kinematical" or "single scattering" approximation.

For an incident plane wave $\psi^{(0)}(\boldsymbol{r}) = exp(-2\pi i \boldsymbol{k}_0 \cdot \boldsymbol{R})$, the first Born approximation for particle waves gives:

$$\psi^{(0)}(\boldsymbol{r}) + \psi^{(1)}(\boldsymbol{r}) = exp(-2\pi i \boldsymbol{k}_0 \cdot \boldsymbol{R}) + \frac{\mu}{4\pi} \frac{exp(-2\pi i k_0 R)}{R} \int \varphi(\boldsymbol{r}') exp(-2\pi i \boldsymbol{G} \cdot \boldsymbol{r}') d\boldsymbol{r}'. \qquad (6)$$

$\varphi(\boldsymbol{r})$ is the potential function, μ is a parameter which specifies the strength of the interaction with potential field. It is not limited in its application to the scattering from single atoms but may be applied to any collection of scattering matter. Normally we think in terms of assemblies of indistinguishable atoms although for X-rays $\varphi(\boldsymbol{r})$ is replaced by the electron distribution, $\rho(\boldsymbol{r})$, and for photonic crystals $\varphi(\boldsymbol{r})$ is replaced by the dielectric constant distribution, $\varepsilon(\boldsymbol{r})$.

The diffraction of light by colloidal crystals is analogous to the diffraction of X-rays by atomic crystals. For convenience, we use the notation appropriate to X-ray diffraction in crystals with the understanding that exactly the same considerations apply for light scattering in photonic crystals within the limits of applicability of the kinematical approximation. The electron density of a collection of atoms can be written as:

$$\rho(\boldsymbol{r}) = \sum_i \rho_i(\boldsymbol{r}) * \delta(\boldsymbol{r} - \boldsymbol{r}_i) \qquad (7)$$

where $\rho_i(\boldsymbol{r})$ is the electron density associated with the atom centered at $\boldsymbol{r} - \boldsymbol{r}_i$ and is not necessarily assumed to be the same as for a free atom.

The assumption of kinematical scattering approximation implies that the amplitude of the single scattered radiation is very small compared with the incident beam amplitude. Then the amplitude of the doubly- and multiply-scattered radiation is much smaller and negligible compared with the single scattered light amplitude.

In reciprocal space, equation (7) is related to a distribution $F(\boldsymbol{u})$ by the Fourier transform:

$$F(\boldsymbol{u}) = \int d\boldsymbol{r}\, \rho(\boldsymbol{r}) \exp(2\pi i \boldsymbol{u}\cdot\boldsymbol{r}) \qquad (8)$$

And if an electron density distribution, $\rho(\boldsymbol{r})$, is considered to be the sum of the distribution $\rho_i(\boldsymbol{r})$ attributed to individual atoms as shown in equation (8) and also define:

$$f_i \overset{\text{def}}{\equiv} \int d\boldsymbol{r} \rho_i(\boldsymbol{r}) \exp(2\pi i \boldsymbol{u}\cdot\boldsymbol{r}) \qquad (9)$$

then Fourier transform of (8) ends up being:

$$F(\boldsymbol{u}) = \sum_i f_i(\boldsymbol{u}) \exp(2\pi i \boldsymbol{u}\cdot\boldsymbol{r_i}) \qquad (10)$$

Construction of Ewald sphere

The geometry of kinematical scattering can be revealed in the so called Ewald sphere.

In equation (6), the scattered amplitude is given in the asymptotic limit of large R, which is known as the Fraunhofer diffraction, as a function of $\boldsymbol{G} = \boldsymbol{k} - \boldsymbol{k}_o$;

$$\psi(\boldsymbol{G}) = -\left(\frac{\mu}{4\pi}\right) \int d\boldsymbol{r}\, \varphi(\boldsymbol{r}) \exp(-2\pi i \boldsymbol{G}\cdot\boldsymbol{r}) \qquad (11)$$

In the appropriate units and putting $\boldsymbol{G} = -\boldsymbol{u}$, we have $\psi(\boldsymbol{G}) = F(\boldsymbol{u})$, and the intensity of scattering light is

$$I(\boldsymbol{G}) = \psi(\boldsymbol{G})\psi^*(\boldsymbol{G}) = \int d\boldsymbol{r}\, P(\boldsymbol{r}) \exp(2\pi i \boldsymbol{u}\cdot\boldsymbol{r}) \qquad (12)$$

where $P(\boldsymbol{r})$ is the Patterson function, which is defined as the Fourier transform of $|F(\boldsymbol{G})|^2$ in this case. Thus for an incident monochromatic beam in a direction defined by the wave vector $\boldsymbol{k}_o$, the intensity diffracted elastically in a particular direction defined by wave vector $\boldsymbol{k}$ is equal to the value of the function $|F(\boldsymbol{G})|^2$ at the position in reciprocal space defined by $\boldsymbol{G} = \boldsymbol{k}_o - \boldsymbol{k}$.

This relationship is visually expressed by the Ewald sphere construction in reciprocal space, shown in Fig. 3. A vector of modulus λ^{-1} (= $|\boldsymbol{k}_o|$) is drawn to the origin, O, of reciprocal space, in the direction of $\boldsymbol{k}_o$ from

the point P. A sphere of radius λ^{-1} is drawn around P as center. Then for any point on the sphere, $\boldsymbol{G}$, the radial vector (module λ^{-1}) from P represents the direction of the diffracted beam $\boldsymbol{k}$ such that $\boldsymbol{G} = \boldsymbol{k} - \boldsymbol{k}_o$. The intensity of the diffracted beam is $|F(\boldsymbol{G})|^2$. Thus this Ewald sphere construction gives the possible directions and intensities of all diffracted beams produced for a given incident beam.

According to the Ewald sphere construction, we see that the geometric condition to be satisfied is

$$\boldsymbol{G} = \boldsymbol{k} - \boldsymbol{k_o} = h\boldsymbol{b_1} + k\boldsymbol{b}_2 + l\boldsymbol{b}_3 \qquad (13)$$

And we can write this in terms of the projections of $\boldsymbol{G}$ onto the real space axes as the well-known "Laue conditions" for diffraction:

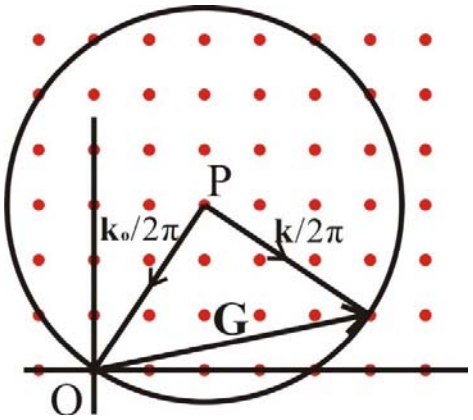

Fig. 3. The Ewald sphere construction.

$$\boldsymbol{G} \cdot \boldsymbol{a}_1 = 2\pi h, \;\; \boldsymbol{G} \cdot \boldsymbol{a}_2 = 2\pi k, \;\; \boldsymbol{G} \cdot \boldsymbol{a}_3 = 2\pi l \qquad (14)$$

It is easy to see in the case of rectangular crystal system, that the perpendicular distance d_{hkl} between planes of the (hkl) set is

$$\left(\frac{1}{d_{hkl}}\right)^2 = \frac{h^2}{|\boldsymbol{a}_1|^2} + \frac{k^2}{|\boldsymbol{a}_2|^2} + \frac{l^2}{|\boldsymbol{a}_3|^2} \qquad (15)$$

Hence from equation (14) and (15), the condition that a sharp diffraction beam should be generated is

$$|\boldsymbol{G}| = 2\pi/d_{hkl} \qquad (16)$$

since $|\boldsymbol{k}_o| = |\boldsymbol{k}| = \lambda^{-1}$, and the angle between $\boldsymbol{k}$ and $\boldsymbol{k}_o$ is 2θ, where θ is the incident glancing angle on (hkl) plane, we have

$$\lambda = 2\, d_{hkl} \sin\theta_{hkl} \qquad (17)$$

which is identical to the Bragg's law. The condition that $\boldsymbol{G}$ should be perpendicular to the lattice planes, which is equivalent to Bragg's concept of regarding the lattice planes as reflection mirrors.

1.2.3. Dynamical Diffraction Theory

The kinematical diffraction theory assumes no change of the incident beam as it propagates through the crystal medium. In other words, the contribution to the electric field inside the crystal medium coming from the diffracted waves is neglected. However, the diffracted waves depend on the internal incident wave which in turn depend on the diffracted waves. Hence the incident and the diffracted waves form a coupled system. The general theory of diffraction in crystals becomes a problem in dispersion theory and is therefore commonly referred to as the dynamical theory of diffraction. And the kinematical diffraction theory is an approximation to the dynamical diffraction theory in the limit of small crystals.

The dielectric constant ε and the polarizability per volume α have the relationship shown as:

$$\varepsilon = 1 + \frac{4\pi\,\alpha}{1-\frac{4\pi}{3}\alpha} \approx 1 + 4\pi\,\alpha \qquad (18)$$

α is a function of position having the periodicity of the lattice, we introduce the symbol ψ (which we should be careful to distinguish from wave function $\psi(\boldsymbol{r})$) for the function $4\pi\alpha$:

$$\psi = 4\pi\,\alpha = \sum_{\mathrm{H}} \psi_{\mathrm{H}}\; \mathrm{e}^{-\mathrm{i}2\pi\mathbf{G}_{\mathrm{H}}\cdot\mathbf{r}} \qquad (19)$$

$$\psi_{\mathrm{H}} = \frac{1}{\mathrm{V}}\int_{\mathrm{V}}\; \mathrm{d}v\; \psi\, \mathrm{e}^{-\mathrm{i}2\pi\mathbf{G}_{\mathrm{H}}\cdot\mathbf{r}} \qquad (20)$$

V is the volume of the unit cell, ψ_{H} is the Fourier coefficient. ψ'_H and ψ''_H are used to represent the real and imaginary parts of the Fourier coefficients respectively.

The square of the refractive index n is equal to the dielectric constant, hence, since ψ is a small quantity,

$$n = 1 + \frac{1}{2}\psi \tag{21}$$

Because ψ is complex, $\psi = \psi' + i\psi''$, the refractive index is also complex, which implies the scattering can be accompanied by absorption. The imaginary part of the refractive index, $\frac{1}{2}\psi''$, is also called the absorption index, and it is related to the linear absorption coefficient μ (for true absorption) by the following equation

$$\mu = -\frac{2\pi\,\psi''}{\lambda_o} \tag{22}$$

In the non-absorbing case, the imaginary part of the refractive index can be neglected. And ψ becomes a pure real function. The maximum diffracted intensity according to the dynamical diffraction theory occurs at an angle θ_m in the crystal given by

$$\theta_m = \theta_B + \frac{1-b}{2b\sin 2\theta_B}\psi_o' \tag{23}$$

where θ_B is the ideal Bragg angle; b is the ratio of the direction cosines of the incident and diffracted wave, which is defined as:

$$b = \frac{\gamma_0}{\gamma_H} = \frac{\boldsymbol{n}\cdot\boldsymbol{u}_o^G}{\boldsymbol{n}\cdot\boldsymbol{u}_H^G} \tag{24}$$

here, $\boldsymbol{n}$ is the surface normal, γ_0 and γ_H are the direction cosines of the incident and diffracted wave, respectively.

For Bragg diffraction, b is a negative value and close to unity. As a result, the profile of the diffracted intensity is centered around the ideal Bragg angle, which, however, is always smaller than the angle that predicted by the Bragg's law in equation (17). In other words, the Bragg's equation is not perfectly satisfied at the center of diffraction pattern.

Considering the Laue method in measuring diffracted intensity, the maximum diffraction intensity would appear at the wavelength:

$$\lambda_m = \lambda_B - \lambda_B \frac{1-b}{4b\sin^2\theta_B}\psi_o' \quad (25)$$

here, λ_B is the diffraction wavelength predicted by Bragg's law. Thus, the dynamical theory predicts a red shift of the diffraction peaks.

The dynamical diffraction theory considers the incident and diffracted beams as a coupled system, and predicts that the diffraction condition differs from the ideal Bragg condition, which is predicted by the kinematical diffraction theory. Our group have theoretically and experimentally studied the dynamical diffraction from CCAs [26].

1.3. Raman Imaging

Raman Imaging is a hyperspectral imaging technique for material characterization. The main purpose of utilizing Raman imaging in material characterization is that most materials have spatially heterogeneity in composition and structure. There is a need to measure the spectra of materials in two and three dimensions, so as to fully understand the composition distribution. Current Raman imaging technique not only provides the visual perception of digital imaging technology, but also gives molecular information from Raman scattering. In a radical definition, Raman image is a bundle of Raman spectra with spatial accuracy [27].

Raman imaging data records the molecular specific Raman scattering from a highly heterogeneous material. Raman imaging measurement will generate a huge amount of independent, spatially resolved Raman spectra. The data of Raman imaging is known as a hyperspectral data cube, which consists two spatial dimensions and a dimension of Raman shift wavenumber. Fig. 4 shows an example of Raman imaging data cube [28]. The information of each pixel can be extracted and studied in detail. Raman imaging measurement provides a comprehensive way to spatially study materials, the technique also reduces the work of sample preparation.

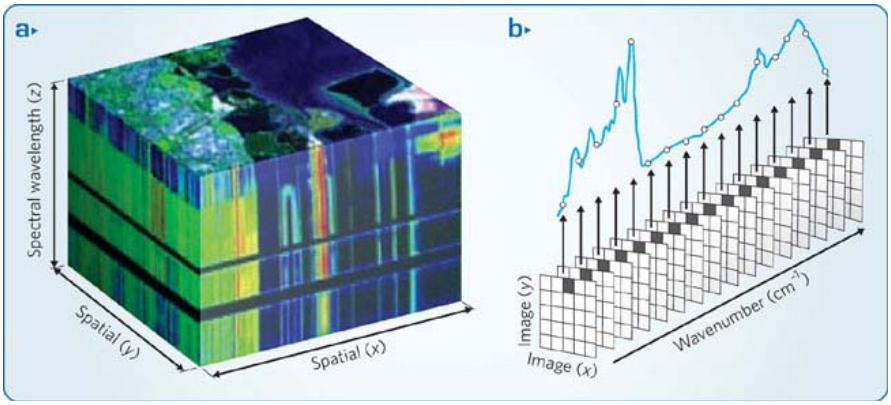

Fig. 4. a) Hyperspectral data cube, b) hyperspectral data cube viewed as a function of wavelength. (From Ref. 28)

Raman images can be generated by scanning the sample surface with a laser beam which is focused on the surface and collecting the Raman spectra at each spatial location. The scanning methods contain point-by point scanning, which utilizes a small spot laser beam; line scanning, in which the laser beam is elongated in on dimension, and wide-field imaging, which collect a whole frame of spectra and analyze with computer to get the hyperspectral data [27].

However, most of the current Raman imaging instruments utilize a dispersive spectrograph or an interferometer, which is huge in size [29]. The disadvantage of huge size and heavy weight makes it impossible to make portable Raman imaging devices, which limits the usage of this technology. Fortunately, our CCA filters can operate as a wavelength-selecting optic, which makes it possible to replace the dispersive grating [27]. Also, the CCA filters do not need as large as the space a dispersive grating needs to perform. Moreover, the high selectivity and diffraction efficiency makes it promising to build a revolutionary Raman imaging spectrometer with smaller size by utilizing our CCA filters as Rayleigh rejection filter and wavelength-selecting filter in deep UV regions. We proposed to build a stand-off Raman imaging spectrometer, the scheme of the setup is shown in Fig. 5. In the work here, I am going to set up a simplified spectrometer without the telescope part, which is shown later in Fig. 8.

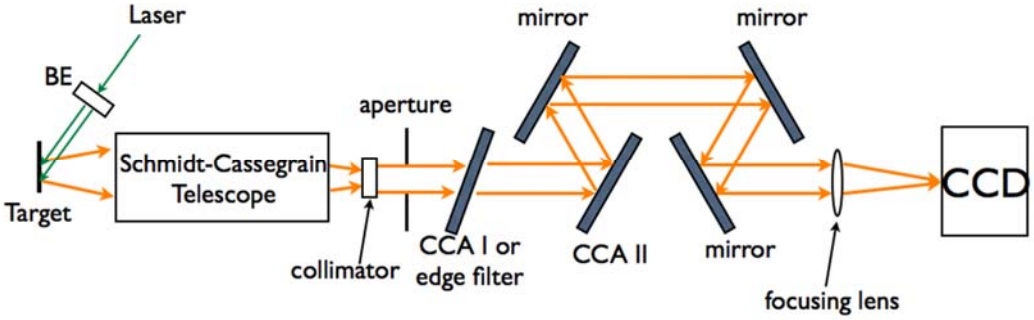

Fig. 5. Scheme of the Raman Imaging spectrometer setup.

2. Experiment Section

2.1. Preparation of CCA Filter

2.1.1. Colloidal Particle Synthesis

Highly charged monodispersed polystyrene and silica particles are synthesized as the materials for fabricating visible CCA filters and deep UV CCA filters, respectively.

2.1.1.1. Polystyrene Colloidal Particles Synthesis

I synthesized PS particles according to the previously reported method by our group [30]. 0.171 g of sodium bicarbonate was dissolved in 138 mL ultra pure water. The solution was deoxygenated by bubbling with nitrogen for 40 min under mechanical stirring at a rate of 350 rpm. After thorough deoxygenation, 2 g of surfactant Aerosol MA-80-1, dissolved in 10 mL of water, was added and the temperature was increased to 50^{o}C. Previously deinhibited and deoxygenated styrene was injected at a rate of 4 mL/min. 2.8 g of COPS-1 was dissolved in 10 mL of water and was injected 5 min after the addition of styrene was completed. The temperature was increased to 70 ^{o}C (±1 ^{o}C), at which point the solution of 0.75 g of ammonium persulfate in 5 mL of water was injected. The reaction was left to reflux for 24 h. Nitrogen blanket and a steady stirring rate of 350 rpm were maintained throughout the reaction.

After the completion of the reaction, the product colloidal was cooled at ambient temperature. Then it was filtered through nylon mesh and was dialyzed against ultra pure water, which was replaced at least twice a day for 2-3 weeks. Ion-exchange resin was added to the solutions for storage.

2.1.1.2. Silica Colloidal Particle Synthesis

Monodisperse, small silica particles were fabricated by using a modified Stöber method [21]. In this modified Stöber method, 8 mL ammonium hydroxide (29.6 wt%) was added to 190 mL ethanol and the

mixture was stirred for 5 min to confirm well mixed. 5 mL tetraethoxysilane (TEOS), dissolved into 10 mL of ethanol, was dropped into the mixture. The reaction mixture was sealed and stirred for 24 h.

The resulting silica dispersion was surface functionalized with the low deep UV absorpting silane coupling agent, 3-(trihydroxylsilyl)-1-propane-sulfonic acid (THOPS, 30% in water). 200 mL of ultra pure water was slowly added to the Stöber silica dispersion under stirring. The mixture was first heated to 50 ^{o}C for ~30 min, followed by heating to 80 ^{o}C for ~1h. Then 6 mL of the silane coupling agent THOPS, which was adjusted to pH ~6 with ammonium hydroxide, was dropped into the silica dispersion. The reaction was refluxed for 6 h at 80 ^{o}C.

The functionalized silica particles were centrifuged and washed with ultra pure water 6 times and redispersed in water to obtain the demanded particle concentration. Ion-exchange resin was added to the colloidal solutions for storage.

2.1.2. CCA Filter Preparation

The colloidal solution concentration was adjusted in order to Bragg diffract light at the desired wavelength regions. The solution was filtered with glass wool to remove the resin, and with a 0.45 μm filter to remove small aggregates.

The CCA filter cell is shown in Fig. 7a. The cell consisted of two fused silica quartz discs (2" dia. x 3/16") separated by a ~125 μm thick Parafilm spacer. The filtered colloidal solution was carefully injected into one of the holes in the quartz disc to fill the cell, in order to avoid bubbles. The particles self assembled into a CCA between the two quartz discs. Shear-flow was also applied to the system to help form a good CCA.

2.2. Characterization of Particles and CCA Filters

2.2.1. Characterization of Colloidal Particles

Particle sizes of both polystyrene and silica particles were measured using dynamic light scattering (DLS) and transmission electron microscopy (TEM) (FEI Morgagni TEM). DLS and zeta potential were measured by using a ZetaPlus (Brookhaven Instruments Corportion). The particle charge densities were measured by conductometric titration (794 Basic Titrino).

2.2.2. UV/Vis Photometer Characterization

Optical diffraction measurements of the CCA filters were performed by using a UV/vis/NIR spectrophotometer. The transmission spectra of CCAs for an incident glancing angle of 90^{o} were measured.

2.2.3. Laser Test

The rejection bandwidth determined from the UV/Vis spectrophotometer measurements are broader than the true CCA bandwidth because the absorption spectrophotometer utilizes a somewhat focused exciting beam. The measured attenuation is also artificially decreased. [21] So a well collimated argon laser was utilized to measure the CCA rejection efficiency of the silica CCA filter.

2.2.3.1. Laser Test with Ocean Optics Spectrometer

The measurement setup is shown in Fig. 6. The 244 nm line of a continuous-wave UV argon laser (Innova 300 FReD, Coherent Inc.) was used as the light source. The laser beam was expanded by using a focusing lens 1, and collimated into a ~1 cm diameter spot by focusing lens 2 before incidence the CCA filter. The CCA filter was mounted on a rotation stage and titled to the Bragg angle, at which the CCA filter Bragg diffracts the laser beam. The transmitted light was collected by focusing lens 3 and detected with a fiber optic probe, connected to Ocean Optics spectrometer. The diffracted beam was also detected similarly.

Diffuse scattered light was detected by setting the probe at a stationary position which was ~30 degrees off the incident beam. Fig. 6b schematically shows the experimental geometry.

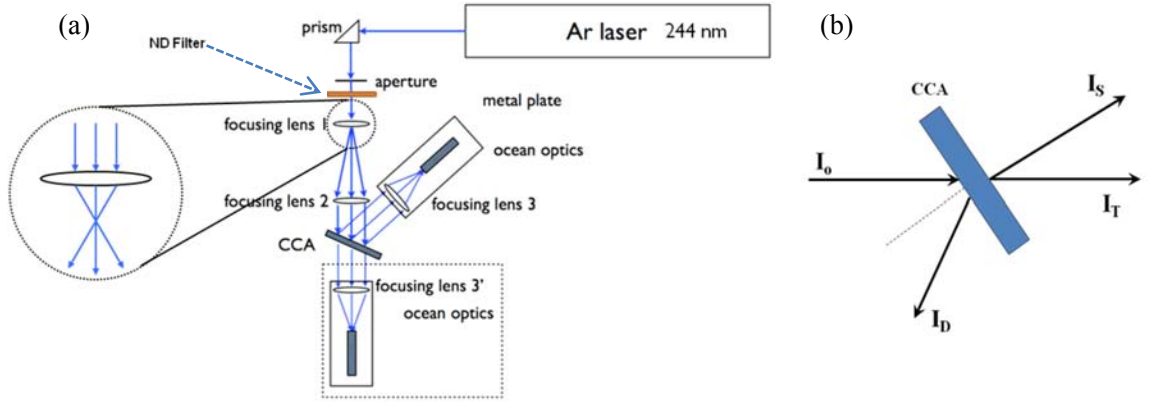

Fig. 6. a) the measurement set-up; b) a scheme of measurement set-up, the scattered light is measured at ~30 degree from incident beam.

The angular dependence of CCA diffraction was also measured by titling the incident angle about the Bragg condition and measuring the intensity of diffracted, transmitted and diffuse scattered light.

2.2.3.2. Teflon Raman Spectrum Measurement

Deep UV Raman spectra of highly scattering Teflon with excitation at the 244 nm line by the same continuous-wave UV argon laser were measured. The laser excited the Teflon sample with the laser beam focused to a ~20 μm diameter spot in a backscattering geometry. Fig 7b shows the optical schematic of the experimental geometry and Triplemate monochromator used for the Raman measurements. [21] The CCA filter was placed between the collection and imaging lens where the light is collimated. The CCA filter was aligned to reject a portion of the Rayleigh scattered light, which allows us to make quantitative determinations of the CCA laser light attenuation. The spectrometer setups were identical for Raman spectral measurements in the absence and presence of the CCA filter.

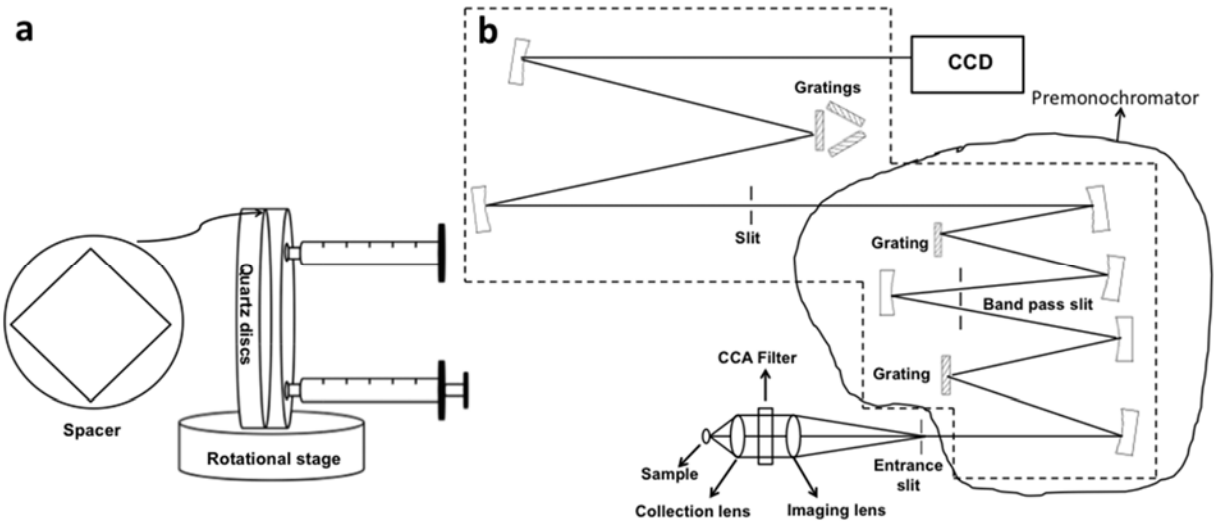

Fig. 7. a) A CCA flow cell for transmission measurements; b) Schematic of triple-stage monochromator for Raman measurements. (From Ref. 21)

2.3. Visible Imaging Experiment

The setups for a visible imaging test are shown in Fig. 8. 514.5 nm argon laser beam (Innova 300 FReD, Coherent Inc.) was introduced onto a piece of fluorescence paper, and the dispersed light was collected by a focusing lens. The Rayleigh scattered light was rejected by the first CCA filter, that was orientated such that the Rayleigh scattered light was Bragg diffracted. The second CCA filter was used to select the wavelength we were interested in while transmitting the adjacent wavelengths. The Bragg diffracted light from the second CCA was reflected by a mirror and imaged on a white screen or detected with Ocean Optics fiber probe. The transmitted light was also imaged on a white screen or detected by Ocean Optics fiber probe.

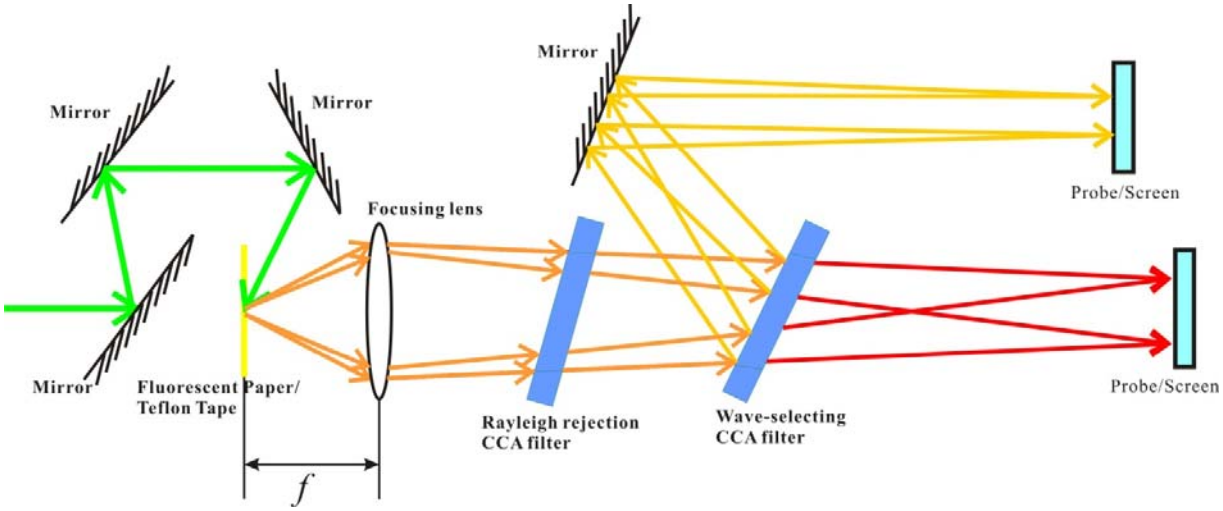

Fig. 8. Setups of visible fluorescence/Raman imaging tests. The object length f is between f_0 and $2f_0$, where f_0 is the focal length of the focusing lens.

3. Results and Discussion

3.1. Colloidal Particle Characterization Results

The TEM images of the polystyrene and silica particles are shown in Fig. 9 and Fig. 10. The modified Stöber method utilizes aqueous ammonium hydroxide solution instead of saturated alcoholic solution of ammonia [31]. Thus, no more water is needed. The typical recipe yielded silica particles with a diameter 44.7 ± 4.3 nm as determined from TEM image (Fig. 9a). The diameter measured by DLS was 59.7 ± 0.5 nm (polydispersity 0.017). The TEM diameter is smaller than that measured by DLS, because DLS measures the hydrodynamic diameter, while TEM measures the diameter of dehydrated particles. Moreover, the hydrated particles also present smaller diameter deviation.[21]

Fig. 9b shows the TEM image of functionalized silica particles, the diameter is 47.9 ± 4.5 nm. The diameter measured by DLS was 62.3 ± 0.4 nm. The zeta potential of the charged particles is -45.3 mV at pH 4.0, which indicates high surface charge. We also determined the surface charges of these silica particles by utilizing conductrometric titration with 0.01 N NaOH. The typical recipe yields 4960 charges per silica particle (11.0 $\mu C/cm^2$).

The synthesized Stöber silica particles without surface functionalization do not have sufficient surface charge to self assemble into CCA; the pK_a of the surface -SiOH is relatively high (~7.1) [32]. The zeta potential of these Stöber silica particles without surface functionalization is only about -16.7 mV at pH 4.0. Wang *et al.* [21] developed a facile and robust method to attach strong sulfonic acid groups ($-SO_3H$) to the surface of the silica colloids in our group by using THOPS as the coupling agent. THOPS was attached to the silica particle surface by a condensation reaction between the surface silanol groups (-SiOH) and that of THOPS. The functionalized silica particles are highly charged due to the low pK_a (<1) of the surface sulfonic acid groups [33]. After cleaning and ion-exchange, the surface functionalized silica particles self-assembled into CCAs.

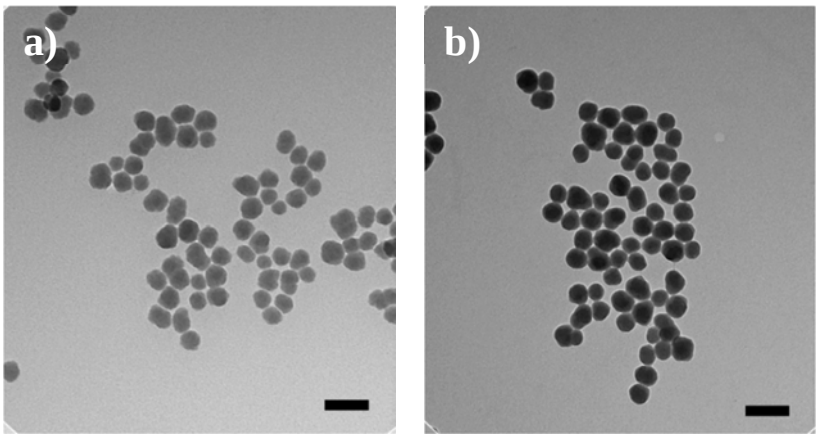

Fig. 9. TEM image of silica particles a) before surface functionalization, b) after surface functionalization. The scale bar is 100 nm.

Monodisperse, highly charged polystyrene particles were also synthesized by using a certain recipe. Fig. 10 shows the TEM image of the resulting polystyrene particles. The diameter is about 96.8 nm measured from TEM image, and 110.2 nm from DLS measurement. The polystyrene particles are highly charged because of the surface sulfate groups which are attached during the PS particles synthesis by the free radical emulsion polymerization [34, 35, 36] as well as the addition of COPS-1, a sulfonated comonomer. The surface charge of polystyrene particles is also determined by utilizing conductrometric titration with 0.01 N NaOH. The typical recipe yields 64580 charges per particle (3.51 μC/cm^2). The particles synthesized here show comparable properties with those reported previously in our group [21, 30].

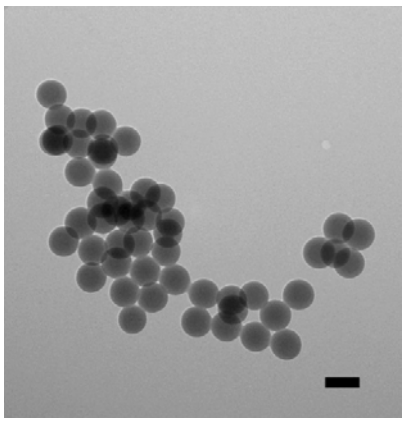

Fig. 10. TEM image of monodisperse highly charged polystyrene particles. The scale bar is 100 nm.

3.2. CCA Filter Characterization Results

3.2.1. Transmission Measurements of CCAs with UV/Vis/NIR Photometer

Both of the highly charged PS and silica particles self assemble into CCAs after cleaning and ion-exchange. The PS CCA filters show iridescent colors because visible light is diffracted, however, silica CCA filters only diffract light in deep UV range, as a result, the silica CCA filters appear to be visually transparent.

Fig. 11 shows the absorbance spectrum of a visible PS CCA filter for incident glancing angle at 90 degree, which shows the rejection band. The rejection band was tuned to ~578 nm by diluting the PS CCA concentration to ~3.6 wt%. This absorbance spectrum indicates a transmission of ~1% at the rejection maximum, while the transmission of adjacent wavelengths is relatively high. For normal incidence, the full bandwidth at half maximum (FWHM) is about 7 nm. However, because the absorption spectrophotometer utilizes a somewhat focused exciting beam, the bandwidth of the rejection band measured here was broadened, and the rejection efficiency was decreased. As the filter was angle-tuned, the CCA filter showed only slight broadening of the rejected FWHM, as well as the decrease of attenuation efficiency [21].

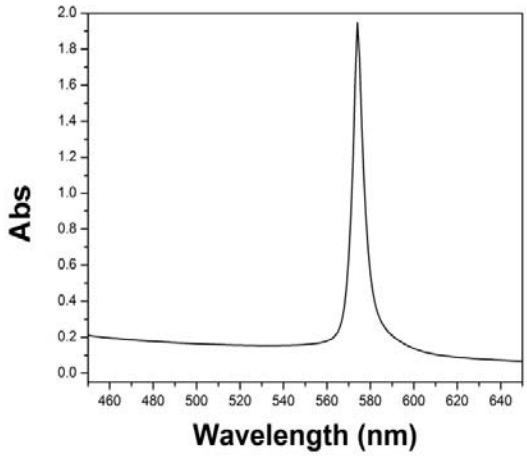

Fig. 11. Extinction spectrum of PS CCA filter measured with UV/Vis/NIR photometer. The diameter of particles here is 96.8 nm. The thickness of CCA is ~125 μm.

Fig. 12 shows the transmission spectrum of silica CCA filter for incident glancing angle at 90 degree. The rejection band is at ~248 nm, and the FWHM is only 4 nm, which is narrower than that previously reported by Wang *et al.* [21]. This spectrum shows the transmission is about 7% at the rejection band maximum.

The bandwidth of the CCA rejection band depends on many factors, such as the degree of ordering of the CCA array, the particle diameter, the thickness of colloidal layers involved in the diffraction, and the refractive index difference between particles and the medium [15, 26, 37, 38]. For these two particles, the bandwidth increased with increasing the sphere diameter [26].

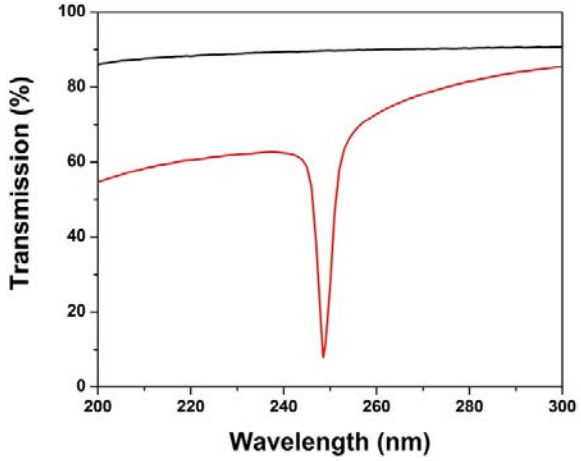

Fig. 12. Transmission spectrum of silica CCA filter measured with UV/Vis/NIR photometer. The black line shows the transmission of filter cell with water.

The transmission spectrum of silica CCA filters shows a relatively low transmittance in the shorter wavelength region. This is because of the disordering of CCA lattice, as well as stacking faults. For our CCA filter, the fcc lattice (111) planes are parallel to the cell surface [14]. Diffraction of the longest wavelength occurs when the incident beam is normal to the (111) planes, this corresponds to the main rejection band in the spectrum. If a CCA sample includes (111) planes with random orientations, which are not parallel with the cell wall, various Bragg diffractions can occur at shorter wavelengths than the main peak. As a result, a decrease in transmittance will occur in shorter wavelength region [39]. The same

phenomenon is also seen in the PS CCA filter, which ends up being relative higher absorbance at shorter wavelength region.

Given the diffraction wavelength at normal incidence measured in these absorbance spectra, the incident angle required for specific wavelength can be calculated from Bragg's and Snell's laws according to equations (26) and (27), where λ_o is the wavelength in air diffracted by the CCA, which depends on the average refractive index of the CCA, n_{avg}, the lattice spacing, d, and the glancing incident light angle, θ, which is the glancing incident angle in the colloidal medium.

$$\lambda_o = 2\, n_{avg}\, d \sin\theta \qquad (26)$$

$$\theta = cos^{-1}[\frac{\cos\theta_o}{n_{avg}}] \qquad (27)$$

The average refractive index of the CCA is calculated by averaging the refractive indices of particles and water according to volume fractions [40]:

$$n_{avg} = \sqrt{\phi_p\, n_p^2 + (1-\phi_p) n_w^2} \qquad (28)$$

where n_p and n_w are refractive indices of particle and water, respectively, $\phi_p$is the volume fraction of particles in the CCA. The glancing angle in the colloidal medium is calculated from Snell's law for refraction, where θ_o is the incident glancing angle at air/quartz interface [26, 41, 42, 43]. Thus, the orientation of CCA can be easily calculated in order to diffract a certain wavelength, λ_o.

3.2.2. Laser Test of Transmission and Angular Dependence of CCA Filter

We measured the transmission of silica CCA filter of Fig. 12 with 244 nm light from an argon laser at the Bragg condition and the angles about the Bragg condition, as well as diffraction and diffuse scattering light intensities. The diffuse scattering light was measured at ~ 30 degree away from the incidence.

Fig. 13 shows that at Bragg condition this CCA filter can attenuate over 99.9% of incident light, a result higher than that of the absorption spectrophotometer measurements. This occurs because the laser light is highly collimated, the result reveals the actual performance of the CCA filter. At the same condition, the filter Bragg reflects ~85.3% of that light, which includes the diffraction from CCA filter and reflection from quartz plate surfaces [44, 45].

The attenuation band in the transmission spectrum is broader than that in the diffraction spectrum of Fig. 13. This is due to the diffuse scattering of the silica particles. According to Rundquist *et al*. [26], this diffuse scattering about the Bragg angle is due to the coherent scattering, which has an angular distribution. The collective motions of the particles, that corresponds to the lattice phonons, give rise to the coherent scattering. This phonon mode of the rigid lattice will cause a distribution of scattered wave vectors around the Bragg angle. And the distribution of scattered wave vectors is the origin of the angular dependence of coherent scattering. At room temperature, the phonon modes of colloidal crystal are the essential cause of the diffuse scattering. The angular distribution of the diffuse scattering is shown in Fig. 13. As a result, the transmission bandwidth broadens. Hurd *et al*. and Tata *et al*. have studied the importance of phonon modes in colloidal crystal light scattering theoretically and experimentally [46, 47].

From the transmission spectrum, we also notice that the attenuation band is relatively broad, the transmission is essentially zero around the Bragg condition. This means, when the filter works as a Rayleigh rejection filter, it has an angular tolerance for the incident light. Thus, even the incident light is not perfectly collimated, the filter can reject merely 99.9% of the Rayleigh light by diffracting and diffuse scattering. On the other hand, when working as a wavelength-selecting filter, the CCA will diffract a narrow band from the spectrum (Fig. 13). However, if the light is not perfectly collimated, the reflection efficiency will not necessarily be 85.3%. Because the some portion of the incident light does not meet Bragg condition, that portion of incident light will not be Bragg diffracted. As a result, the reflection efficiency will be lower than the value measured here.

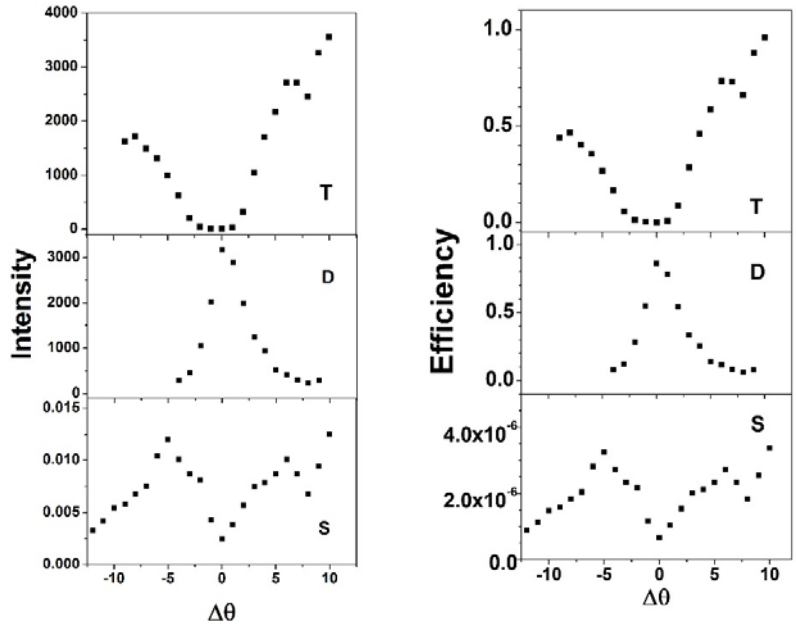

Fig. 13. Plot of transmission, diffraction and scattering intensity and efficiency. Efficiencies were normalized to the incident light intensity. The incident light intensity was measured without any CCAs.

3.2.3. Teflon Raman Spectrum Measurement

The silica CCA filter of Fig. 12 was used to reject the Rayleigh scattered light in 244 nm excited Raman measurements of Teflon. In order to avoid saturating the CCD camera by letting the Rayleigh light through, I adjusted the premonochromator shown in Fig. 7 to block a portion of the Rayleigh scattered light. So that I could still quantitatively measure the Rayleigh rejection efficiency of the CCA filter. The CCA filter was located between the collection and imaging lens where the light is collimated, and was orientated at the certain angle that it would diffract 244 nm Rayleigh light.

In Fig. 14, the high peak of black line is the Rayleigh peak of Teflon spectrum without the silica CCA filter. The shape of the Rayleigh peak looks assymetric, because I changed the premonochromator so that the Rayleigh scattered light was partially blocked. The red line in Fig. 14 is the Teflon Raman spectrum measured with the silica CCA filter at Bragg condition. It shows a significantly attenuated Rayleigh scattering peak because the silica CCA filter Bragg diffracts 244 nm light when at ~85 degree incident

angle orientation. The ratio of integrated peak areas indicates that the CCA filter rejects 99.91% of the Rayleigh scattering light at 244 nm while transmitting the Raman bands of Teflon. However, due to the rejection bandwidth, the Raman bands were also relatively attenuated, which is consistent with the transmission measurement in Fig. 12. The rejection efficiency measured here is higher than that previously reported by Wang *et al.* [21]. However, I did not observe the 290 cm^{-1} and 379 cm^{-1} Raman bands. The absence of these two Raman bands is due to the change of premonochromator.

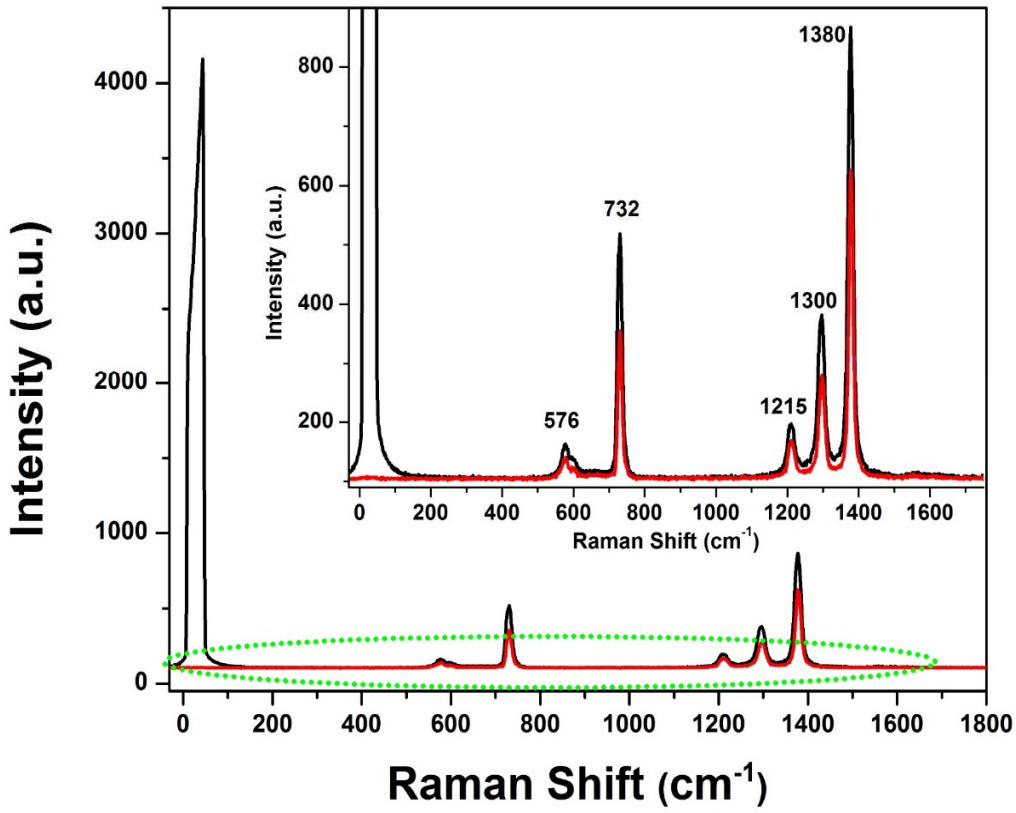

Fig. 14. Teflon 244 nm UV Raman spectra in the absence (black) and presence (red) of the CCA filter at an incident glancing angle of ~85 degree. The inset shows an expansion of the circled region.

3.3. Visible Imaging Results

The PS CCA filter was tuned to ~518 nm at normal incidence by adjusting the particle concentration to ~5.3 wt%. This PS CCA filter was used to reject the Rayleigh scattering line in the 514.5 nm excited fluorescence of a fluorescence paper. Another PS CCA filter (Fig. 11) was used as a wavelength-selecting filter to reflect the band we are interested in the fluorescence spectrum.

In this test, the diameter of the 514.5 nm laser beam on the paper was ~3 mm, so the beam after focusing lens was not perfectly collimated. Fortunately, as discussed above, the CCA filter has an angular tolerance for transmission, which is shown in the transmission spectrum of Fig. 13. Thus, even though the incident light of the Rayleigh rejection filter was not perfectly collimated, it was still able to block over 99.9% of the Rayleigh scattering.

Fig. 15 shows the spectra of light collected by the focusing lens without any CCA filters (Fig. 15a), light after Rayleigh rejection filter (Fig. 15b), light diffracted by wavelength-selecting filter (Fig. 15c) and light after Rayleigh rejection filter and wavelength-selecting filter (Fig. 15d), respectively. It is shown in Fig. 15a that there is a huge band at 514.5 which came from the Rayleigh scattering light from fluorescence paper. When the Rayleigh rejection filter was tuned to Bragg diffract 514.5 nm light, the Rayleigh scattering light was efficiently rejected. So in Fig. 15b, there is no Rayleigh scattering band at 514.5 nm. Even with increased the integration time, we did not observe the Rayleigh scattering band, which indicates great rejection efficiency of our CCA filter.

After rejecting the Rayleigh scattering light from the fluorescence, wavelength-selecting CCA filter was then used to reflect a certain band from the fluorescence light. This diffraction spectrum is shown in Fig. 15c. The band is sharp and narrow and has a FWHM of ~7 nm, which is consistent with the FWHM we found from UV/Vis/NIR spectrophotometer measurement. There is a shoulder peak in Fig. 15c beside the selected band, it was due to the surface reflection of the quartz plates. According to Ref. 40 and Fig. 11, the quartz plate would unselectively reflect ~5% of the incident light [44, 45], which was the whole

fluorescence band. That is why the shoulder peak shows the similar shape as the fluorescence band in Fig. 15a.

Fig. 15d shows the transmission spectrum after both Rayleigh rejection and wavelength-selecting CCAs. It is clear that the rest of fluorescence band adjacent the reflected band was transmitted.

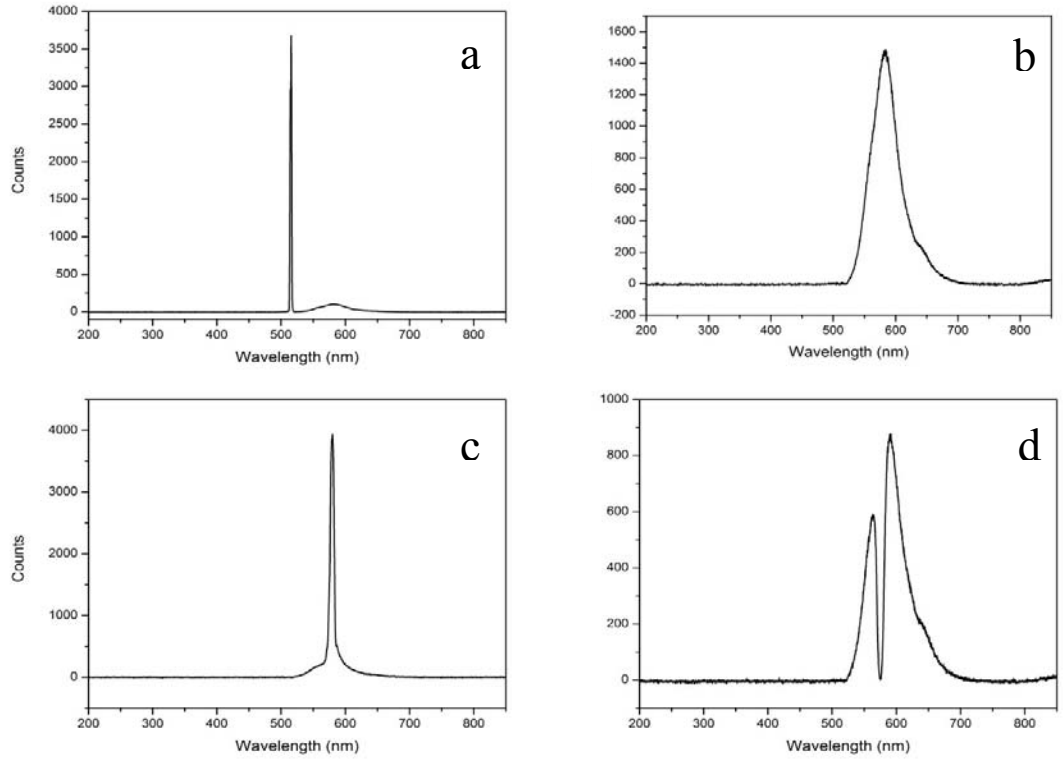

Fig. 15. Spectra measured with Ocean Optics probe: a) Rayleigh scattering light with a broad fluorescence band, b) Transmission light after Rayleigh rejection filter, c) Reflected light from wavelength-selecting CCA filter, d) Transmission light after Rayleigh rejection filter and wavelength-selecting CCA filter. Spectra were taken in different integration times.

Because the light after the focusing lens in Fig. 8 was not perfectly collimated, giving long enough travelling path, we were able to collect images on a piece of paper even without another focusing lens, the images are shown in Fig. 16.

Fig. 16a shows that the laser beam was exciting the fluorescent paper. The beam was hitting at a letter "T" on the paper. In Fig. 16b, without any CCA filters, the image was collected on a piece of white paper,

which came from Rayleigh scattering and fluorescence. The color of the image is a combination of yellow and green, resulting from the 514.5 nm Rayleigh light and the broad fluorescence band. The imaging in Fig. 16b is corresponding to the spectrum in Fig. 15a.

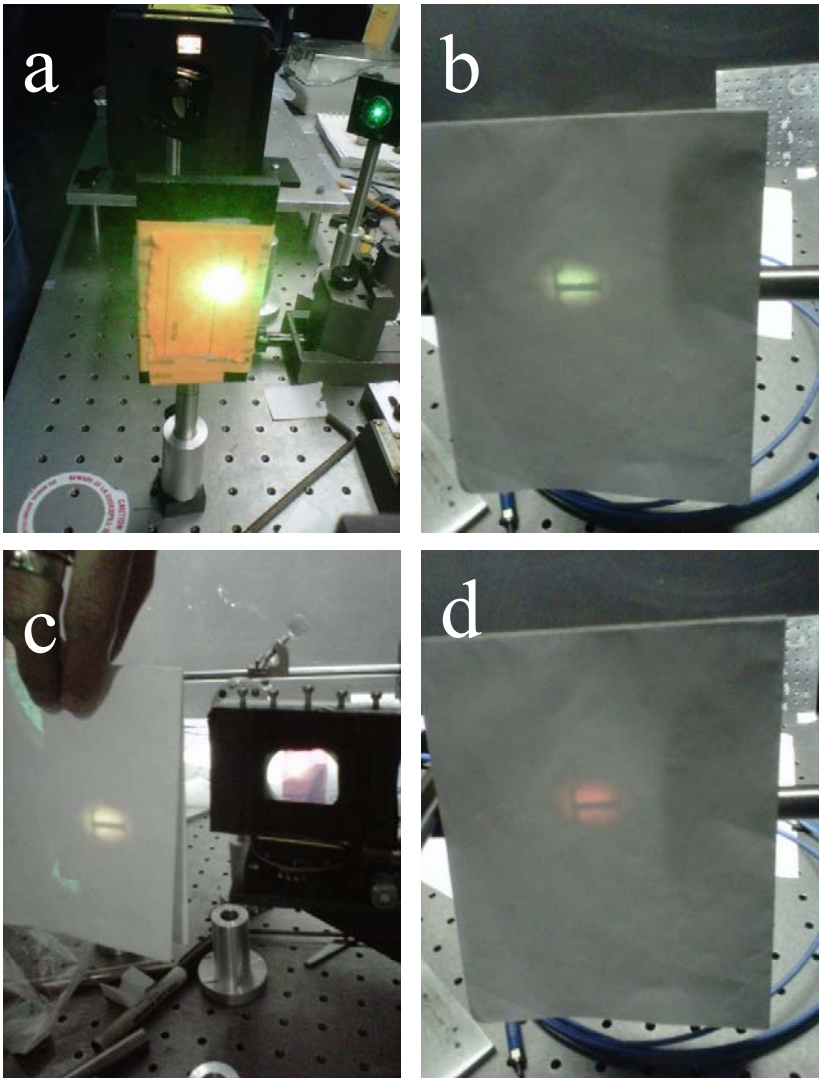

Fig. 16. Images of florescence measurements: a) excite the fluorescence paper with 514.5 nm argon laser line, the beam is hitting on a sideway turned letter 'T" on the paper, b) the image of fluorescence collected on a white paper without any CCA filter, c) the image of the selected band by wavelength-selecting CCA filter, corresponding to Fig. 15c, d) the image collected after Rayleigh rejection filter and wavelength-selecting filter, corresponding to Fig. 15d.

After attenuating the Rayleigh scattering light and selecting wavelength with CCA filters, a narrow band of fluorescence light was collected, which is shown in Fig. 16c, the image was in orange color. This image

in Fig. 16c is corresponding to the spectrum in Fig. 15c. At the meantime, the transmitted light was collected after the two CCA filters, showing a red image in Fig. 16d, which corresponds to the spectrum of Fig. 15d. Because the Rayleigh scattering and shorter wavelength were both rejected, the transmission image was at longer wavelength, giving the red color.

In all the images collected here, the sideway turned letter “T” shows no color, because the ink of letters is not fluorescent. However, the surrounding of the sideway turned letter “T” shows different colors due to the fluorescent paper. The images visually reflect the spatial distribution of the fluorescent material and non-fluorescent material at the illuminated spot.

The test here demonstrated the possibility to develop an imaging spectrometer with CCA filters. The setups for fluorescence imaging here are also promising for Raman imaging measurement.

4. Conclusion and Future Work

4.1. Conclusion

In the work here, small monodisperse, highly charged polystyrene and silica particles were synthesized. These particles self assembled into crystalline colloidal arrays in low ionic strength due to the repulsive force between particles. These CCAs are able to Bragg diffract incident light with certain wavelength. With proper concentration of particles, we fabricated polystyrene CCA for diffracting visible light and silica CCA for diffracting deep UV light.

The visible and UV CCA filters showed great attenuation and Bragg diffraction efficiency, and very narrow rejection bands. The laser transmission measurement was taken, showing the transmission angular dependence of silica CCA filter about Bragg condition. The diffusive scattering revealed the phonon modes of the CCA lattices. Teflon Raman measurement was also performed with the silica CCA Rayleigh rejection filter. The silica CCA filter showed significant attenuation of the Rayleigh scattering, while transmitting the adjacent Raman bands with low attenuation.

At last, fluorescence imaging was demonstrated with visible polystyrene CCA utilized as a Rayleigh rejection filter and wavelength-selecting filter. We were able to reject the Rayleigh scattering light and select the band we interested in and collected images on screens. It is very promising to build a Raman imaging spectrometer utilizing CCA filters.

4.2. Future Work

The performance of CCA filter depends on many factors as mentioned above, such as the monodispersity of particles, the degree of ordering of particle arrays within the CCA, the particle diameter, the thickness of colloidal layers that involve in the diffraction, and the difference between the refractive indices of the particles and medium. In order to optimize our CCA filter, there is a lot of work we can do. The silica particles in Fig. 9 were not highly monodisperse, the TEM measurement showed a deviation about 10%.

According to the Lindemann [48] and Born [49] criteria of melting, the CCA was in a pseudo-crystalline state even without any thermal motion. Thus, synthesizing highly monodisperse silica particles could be essential for making better deep UV CCA filters. Besides the modified Stöber method described here, microemulsion method has also been used to synthesize small silica particles with uniform morphology (< 4% of deviation) [50, 51, 52]. Microemulsion method has also been tried here, the TEM images are shown in Fig. 17. The particles were very uniform and spherical. However, after surface modification, the particles formed aggregation and the suspension looked milky white instead of transparent. In Fig. 17b, it is clear that some particles have grown together to form aggregates. So we aimed to understand the mechanism of aggregation and overcome this problem to get better silica particles for our CCA filter.

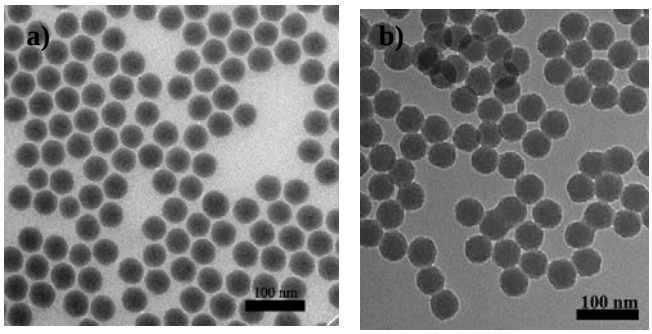

Fig. 17. TEM images of the microemulsion silica particles, a) before modification; b) after modification.

The present silica CCA filter can be easily disrupted and lose ordering by mechanical vibrations or the evaporation of solvent, thus the CCA filter attenuation will decrease, and the bandwidth will broaden. So, in order to make our filter more robust, we will develop methods to solidify the CCA. Also, fabrication solidified DUV filter is an important step to commercialize our Rayleigh rejection filter. We will use physical cross-linked hydrogels to form solidified CCA filter, because the initiator for UV polymerization will absorb deep UV light, thus it will make our system complicated and might ruin the performance of CCA filter.

We will also demonstrate the visible Raman imaging of highly scattering material, such as Teflon with our imaging spectrometer setup. We will utilize a CCD camera instead of the Ocean Optics fiber probe as the detector. With better CCA filters, we are confident to block the Rayleigh scattered light more efficiently. After this, we will demonstrate the deep UV Raman imaging of Teflon on our setup with deep UV CCA filters. The final attempt is to measure explosives with our imaging spectrometer at deep UV range.

5. Reference

[1] Joannopoulos, J. D., et al., *Photonic Crystals: Molding the Flow of Light 2nd Edition*, Princeton Press, 2008.

[2] Yablonovitch, E., *Phys. Rev. Lett.* **58** (20), 2059 (1987).

[3] John, S., *Phys. Rev. Lett.* **58** (23), 2486 (1987).

[4] Jones, J. B.; Sanders, J. V.; Segnit, E. R., *Nature* **204** (4962), 990 (1964).

[5] Kinoshita, S.; Yoshioka, S.; Kawagoe, K., *Proc. R. Soc. London Ser. B* **269**, 1417 (2002).

[6] Forsyth, P. A.; Marcelja, S.; Mitchell, D. J.; Ninham, B. W., *Adv. Colloidal Interface Sci.* **9**, 37 (1978).

[7] Noda, S.; Tomoda, K.; Yamamoto, N.; Chutinan, A., *Science* **289**, 604 (2000).

[8] Dabbs, D. M.; Aksay, I. A., *Annual Review of Physical Chemistry* **51**, 601 (2000).

[9] Lee, K.; Asher, S. A., *J. Am. Chem. Soc.* **122**, 9534 (2000).

[10] Xu, X.; Goponenko, A. V.; Asher, S. A., *J. Am. Chem. Soc.* **130** (10), 3113 (2008).

[11] Reese, C.; Asher, S. A., *Anal. Chem.* **75** (15), 3915 (2003).

[12] Alexeev, V. L.; Sharma, A. C.; Goponenko, A. V.; Das, S.; Lednev, I. K.; Wilcox, C. S.; Finegold, D. N.; Asher, S. A*., Anal. Chem.* **75**, 2316 (2003).

[13] Zhang, J. T.; Chao, X.; Asher, S. A., "Two-Dimensional Array Debye Ring for Molecular Recognition Detection", in preparation, 2012.

[14] Flaugh, P. L.; O'Donnell, S. E.; Asher, S. A., *Appl. Spectrosc.* **38**, 847 (1984).

[15] Asher, S. A.; Flaugh, P. L.; Washinger, G., *Spectroscopy* **1**, 26 (1986).

[16] Zajac, M.; Nowak, J., *Appl. Opt.* **29**, 5198 (1990).

[17] Pelletier, M. J.; Reeder, R. C., *Appl. Spectrosc.* **45**, 765 (1991).

[18] Yang, M.; Morris, M. D.; Michael, D.; Owen, H., *Appl. Spectrosc.* **45**, 1533 (1991).

[19] Semenov, G. B.; Aristov, A. K.; Shchedrunova, T. V.; Varnaev, A. V.; Zhevlakov, A. P.; Grozdilov, V. M., *J. Opt. Technol.* **72**, 196 (2005).

[20] Greenham, A. C.; Nichols, B. A.; Wood, R. M.; Nourshargh, N.; Lewis, K. L., *Opt. Eng.* **32**, 1018 (1993).

[21] Wang, L.; Tikhonov, A.; Asher, S. A., *Appl. Spectrosc.* **66**, 436 (2012).

[22] Kittle, C., *Introduction to Solid State Physics, 3rd Edition* (John Wiley & Sons, Inc., New York, 1968).

[23] Cowley, J. M., *Diffraction Physics, 3rd Edition* (Elsevier Science B. V., Amsterdam, 1995).

[24] Zachariasen, W. H., *Theory of X-ray Diffraction in Crystals* (John Wiley & Sons, Inc., New York, 1945).

[25] http://hays.outcrop.org/GSCI310/lecture8.html

[26] Rundquist, P. A.; Photinos, P.; Jagannathan, S.; Asher, S. A., *J. Chem. Phys.* **91**, 4932 (1989).

[27] Šašić, S.; Ozaki, Y., *Raman, Infrared, and Near-Infrared Chemical Imaging* (John Wiley & Sons, Inc., New Jersey, 2010).

[28] Bannon, D., *Nature Photonics* **3**, 627 (2009).

[29] Boogh, L.; Meier, R.; Kausch, H., *J. Polym. Sci. B*, **30**, 325 (1992).

[30] Reese, C. E.; Guerrero, C. D.; Weissman, J. M.; Lee, K.; Asher, S. A., *J. Colloidal Interface Sci.* **232**, 76 (2000).

[31] Stöber, W.; Fink, J., *J. Colloidal Interface Sci.* **26**, 62 (1968).

[32] Hair, M. L.; Hertl, W., *J. Phys. Chem.* **74**, 91 (1970).

[33] Kwon, Y., *Handbook of Essential Pharmacokinetics, Pharmacodynamics and Drug Metabolism for Industrial Scientists* (Kluwer Academic/Plenum Publishers, New York, 2001), p. 43.

[34] Woods, M. E.; Dodge, J. S.; Krieger, I. M.; Pierce, P. E., *J. Paint Technol.* **40**, 541 (1968).

[35] Dodge, J. S.; Woods, M. E.; Krieger, I. M., *J. Paint Technol.* **42**, 71 (1970).

[36] Papir, Y. S.; Woods, M. E.; Krieger, I. M., *J. Paint Technol.* **42**, 571 (1970).

[37] Tikhonov, A.; Coalson, R. D.; Asher, S. A., *Phys. Rev. B* **77**, 235404 (2008).

[38] Asher, S. A.; Weissman, J. M.; Tikhonov, A.; Coalson, R. D.; Kesavamoorthy, R., *Phys. Rev. E* **69**, 066619 (2004).

[39] Kanai, T.; Sawada, T.; Toyotama, A.; Kitamura, K., *Adv. Funct. Mater.*, **15** (1), 25 (2005).

[40] Fudouzi, H., *Adv. Powder Technol.* **20**, 502 (2009).

[41] Asher, S. A.; Holtz, J.; Liu, L.; Wu, Z., *J. Am. Chem. Soc.* **116**, 4997 (1994).

[42] Krieger, I. M.; O'Neil, F. M., *J. Am. Chem. Soc.* **90**, 3114 (1968).

[43] Hiltner, P. A.; Krieger, I. M., *J. Phys. Chem.*, **73**, 2386 (1969).

[44] Loh, E., *Solid State Commun.* **2** (9), 269 (1964).

[45] http://www.2spi.com/catalog/ltmic/quartz-slides-coverslips.html

[46] Hurd, A. J.; Clark, N. A.; Mockler, R. C.; O'Sullivan, W. J., *Phys. Rev. A* **26**, 2869 (1982).

[47] Tata, B. V. R.; Mohanty, P. S.; Valsakumar, M. C.; Yamanaka, J., *Phys. Rev. Lett.* **93**, 268303 (2004).

[48] Lindemann, F. A., *Z. Phys.* **11**, 609 (1910).

[49] Born, M., *J. Chem. Phys.* **7**, 591 (1939).

[50] Bagwe, R. P.; Hilliard, L. R.; Tan, W. H., *Langmuir* **22**, 4357 (2006).

[51] Chang, S. Y.; Liu, L; Asher, S. A., *J. Am. Chem. Soc.* **116**, 6739 (1994).

[52] Deng, G.; Markowitz, M. A.; Kust, P. R.; Gaber, B. P., *Mater. Sci. Eng.* **11**, 165 (2000).